Y-2440

Y-12

OAK RIDGE Y-12 PLANT

MARTIN MARIETTA

SPECIMEN TYPE AND SIZE EFFECTS ON LITHIUM HYDRIDE TENSILE STRENGTH DISTRIBUTIONS

R. E. Oakes, Jr.

December 1991

MANAGED BY
MARTIN MARIETTA ENERGY SYSTEMS, INC.
FOR THE UNITED STATES
DEPARTMENT OF ENERGY

DISCLAIMER

Y-2440

Distribution Category UC-704

Y--2440

DE92 008200

Y-12 Development Division

SPECIMEN TYPE AND SIZE EFFECTS ON LITHIUM HYDRIDE TENSILE STRENGTH DISTRIBUTIONS

R. E. Oakes, Jr.

December 1991

Prepared by the
Oak Ridge Y-12 Plant
P. O. Box 2009
Oak Ridge, Tennessee 37831-8169
managed by
Martin Marietta Energy Systems, Inc.
for the
U.S. Department of Energy
under contract DE-AC05-84OR21400

CONTENTS

LIST OF FIGURES v

ABSTRACT vii

SUMMARY 1

INTRODUCTION 3

TENSILE STRENGTH DISTRIBUTIONS OF LITHIUM HYDRIDE 6
MATERIAL DESCRIPTION 6
SPECIMEN DESCRIPTIONS 6
Four-Point-Flexure Specimen 6
Ring Tensile Specimen 8
Elliptical-Transition Tensile Specimen 8
Biaxial-Disk-Flexure Specimen 11
EXPERIMENTAL RESULTS, ANALYSIS, AND DISCUSSION 15

CONCLUSIONS AND RECOMMENDATIONS 25

ACKNOWLEDGMENTS 26

REFERENCES 27

APPENDIX A. EFFECTIVE VOLUME AND AREA DERIVATIONS FOR THE RING TENSILE SPECIMEN 29
THE EFFECTIVE VOLUME 29
THE EFFECTIVE AREA 31

APPENDIX B. EFFECTIVE VOLUME AND AREA DERIVATIONS FOR THE ELLIPTICAL-TRANSITION TENSILE SPECIMEN 33
THE EFFECTIVE VOLUME 33
THE EFFECTIVE AREA 35

APPENDIX C. EFFECTIVE VOLUME AND AREA DERIVATIONS FOR THE BIAXIAL-DISK-FLEXURE SPECIMEN 37
THE EFFECTIVE VOLUME 37
THE EFFECTIVE AREA 40
REFERENCE 41

APPENDIX D. LITHIUM HYDRIDE TENSILE STRENGTHS FROM FOUR SPECIMEN TYPES 42

LIST OF FIGURES

Figure		Page
1	Composite lithium hydride strength distributions from axially loaded (elliptical-transition) tensile specimens, hydraulically pressurized ring tensile specimens, four-point-flexure specimens, and concentric-ring biaxial-disk-flexure specimens	4
2	Four-point-flexure (a) specimen geometry and (b) outer-fiber stress profile	7
3	Ring tensile (a) specimen geometry and (b) through-wall circumferential stress profile	9
4	Elliptical-transition tensile (a) specimen geometry and (b) axial stress profile in the gage and transition regions	10
5	Effective area and effective volume [Eqs. (7) and (8)] evaluated for the elliptical-transition tensile specimen of Fig. 4 as a function of Weibull modulus	12
6	Biaxial-disk-flexure specimen geometry and outer-fiber stress profiles. (a) Disk specimen geometry; (b) tensile surface radial-stress profile; and (c) tensile surface tangential-stress profile	13
7	Effective area and effective volume [Eqs. (9) and (10)] evaluated for the biaxial-disk-flexure specimen of Fig. 6 as a function of Weibull modulus	16
8	Composite lithium hydride strength distributions of upper suspensions from four tensile specimen types	17
9	Composite lithium hydride strength distributions of lower suspensions from three tensile specimen types	18
10	Fracture surfaces of two lowest-strength and two highest-strength elliptical-transition tensile specimens, which confirm the association of low-strength failures with surface flaws and high-strength failures with volumetric flaws. (a) Surface-fracture initiation site at 16.9 MPa; (b) surface-fracture initiation site at 21.9 MPa; (c) internal-fracture initiation site at 36.9 MPa; and (d) internal-fracture initiation site at 41.3 MPa	19

LIST OF FIGURES (continued)

Figure		Page
11	Effect of effective volume on characteristic strength for the upper-suspension lithium hydride data.	23
12	Effect of effective specimen surface area on characteristic strength for the lower-suspension lithium hydride data	24
A.1	Definition of volume and surface elements used to derive effective volume and area for the ring tensile specimen. (a) Cylindrical volume element used for risk-of-rupture integration over the range $r = a$ to b; (b) annular surface element used for risk-of-rupture integration for ends and inner and outer surface areas subjected to uniform stresses	30
B.1	Definition of volume and surface elements used to derive effective volume and area for the elliptical-transition tensile specimen	34
C.1	Definition of volume and surface elements used to derive effective volume and area for the biaxial-disk-flexure specimen. (a) Disk and ring volume elements used for risk-of-rupture integrations for center and outer regions of specimen; and (b) inner effective area and outer ring area element used for risk-of-rupture integration for outer region of specimen	38

ABSTRACT

Weibull's two-parameter statistical-distribution function is used to account for the effects of specimen size and loading differences on strength distributions of lithium hydride. Three distinctly differing uniaxial specimen types (i.e., an elliptical-transition pure tensile specimen, an internally pressurized ring tensile, and two sizes of four-point-flexure specimens) are shown to provide different strength distributions as expected, because of their differing sizes and modes of loading. After separation of strengths into volumetric- and surface-initiated failure distributions, the Weibull characteristic strength parameters for the higher-strength tests associated with internal fracture initiations are shown to vary as predicted by the effective specimen volume Weibull relationship. Lower-strength results correlate with the effective area to a much lesser degree, probably because of the limited number of surface-related failures and the different machining methods used to prepare the specimens.

The strength distribution from a fourth specimen type, the predominantly equibiaxially stressed disk-flexure specimen, is well below that predicted by the two-parameter Weibull-derived effective volume or surface area relations. The two-parameter Weibull model cannot account for the increased failure probability associated with multiaxial stress fields.

Derivations of effective volume and area relationships for those specimens for which none were found in the literature, the elliptical-transition tensile, the ring tensile, and the disk flexure (including the outer region), are also included.

SUMMARY

The tensile strength of brittle materials is dependent upon both the size of the specimen being tested and the stress distribution within the specimen. Weibull's two-parameter statistical distribution is used to account for these effects on strength distributions of lithium hydride by using the relationship

$$\frac{\sigma_{0,A}}{\sigma_{0,B}} = \left(\frac{V_{E,B}}{V_{E,A}}\right)^m$$

for failures related to internal flaws or

$$\frac{\sigma_{0,A}}{\sigma_{0,B}} = \left(\frac{A_{E,B}}{A_{E,A}}\right)^m$$

for surface-related flaws,

where

σ_0 = Weibull characteristic strength,
m = Weibull modulus,
V_E = effective volume,
A_E = effective area,
Subscript A and B = specimen types or sizes.

Three distinctly differing uniaxial specimen types (i.e., an elliptical-transition pure tensile specimen, an internally pressurized ring tensile, and two sizes of four-point flexure) are shown to provide different strength distributions as expected, because of their differing sizes and loading modes. After strengths are separated into upper- and lower-strength distributions, the upper-strength distributions from all uniaxial specimen types vary as predicted by the Weibull-based effective specimen volume relationship. The effectiveness of the Weibull-based effective area relationship proved applicable only to low-strength distributions for two specimen types, and this applicability appears to be fortuitous. The association of higher strengths with volumetric and lower strengths with surface failure initiation is confirmed by fractography.

Lower strengths in the distributions are believed to result from surface-machining damage, and the effective area correlation was demonstrated for only two specimen types, the large four-point flexure and the ring tensile, because of an insufficient number of surface-related failures in the remaining specimen types. Different machining methods are required to fabricate the different specimen types, each producing a unique surface finish. Use of Weibull statistics requires identical flaw populations. The grains constitute the major internal flaw source, and the grain size distribution is uniform for all specimens; machining damage constitutes the major surface flaw source and would be expected to vary with the machining methods used.

The two-parameter Weibull model cannot account for increased failure probability associated with the multiaxial stress fields of the fourth specimen type, the predominantly equibiaxially stressed disk-flexure specimen. Alternative theories need to be investigated for a solution to this problem since most components would experience biaxial stresses. Biaxial stresses produce appreciably lower strengths than do uniaxial stresses; thus, scaling from uniaxial-specimen data to biaxially stressed component sizes would provide nonconservative estimates of component strengths.

INTRODUCTION

The tensile strength of a brittle material is controlled by the size and distribution of both surface and internal flaws in the material. Consequently, the tensile strengths of brittle materials exhibit sampling size and loading effects that are substantial in some materials. Larger specimens, which have a greater probability of containing a critical size flaw, exhibit lower strengths than do smaller, geometrically similar specimens. However, loading effects can cause large bend-type specimens to exhibit higher strength values than do physically smaller, uniform-tensile specimens because a smaller portion of the bend specimen, the outer region, is more highly stressed. These effects are well demonstrated by the major differences in strength distributions in Fig. 1 from four widely differing tensile-strength specimen types.

The earliest and still the most widely accepted statistical theory of fracture that quantifies size and loading effects on strength was proposed by Weibull.[1,2] The simplest and most widely used two-parameter formulation of Weibull's approach to describing the probability of failure, P, at a stress, σ, for volumetric flaws is

$$P = 1 - \exp\left[-\int_V \left(\frac{\sigma}{\sigma_0}\right)^m dV\right], \tag{1}$$

where the integral is the volumetric risk of rupture,

$$B_V = \int_V \left(\frac{\sigma}{\sigma_0}\right)^m dV . \tag{2}$$

Equation (2) is integrated throughout the entire volume that is subjected to tensile stress. The quantity σ_0 is the size-dependent characteristic strength (at $P = 63.2\%$) for the distribution, and the exponent m is the size-independent Weibull modulus, representing scatter in the strength data and a measure of the flaw density of the material. High m values, such as those existing in common metals, minimize size and loading effects in strength distributions.

When surface-related flaws are responsible for failure, Eq. (1) can be rewritten as

$$P = 1 - \exp\left[-\int_A \left(\frac{\sigma}{\sigma_0}\right)^m dA\right],$$

where now the surface risk of rupture B_A is evaluated over all tensile-stressed surface areas, with A and dA replacing V and dV in Eq. (2).

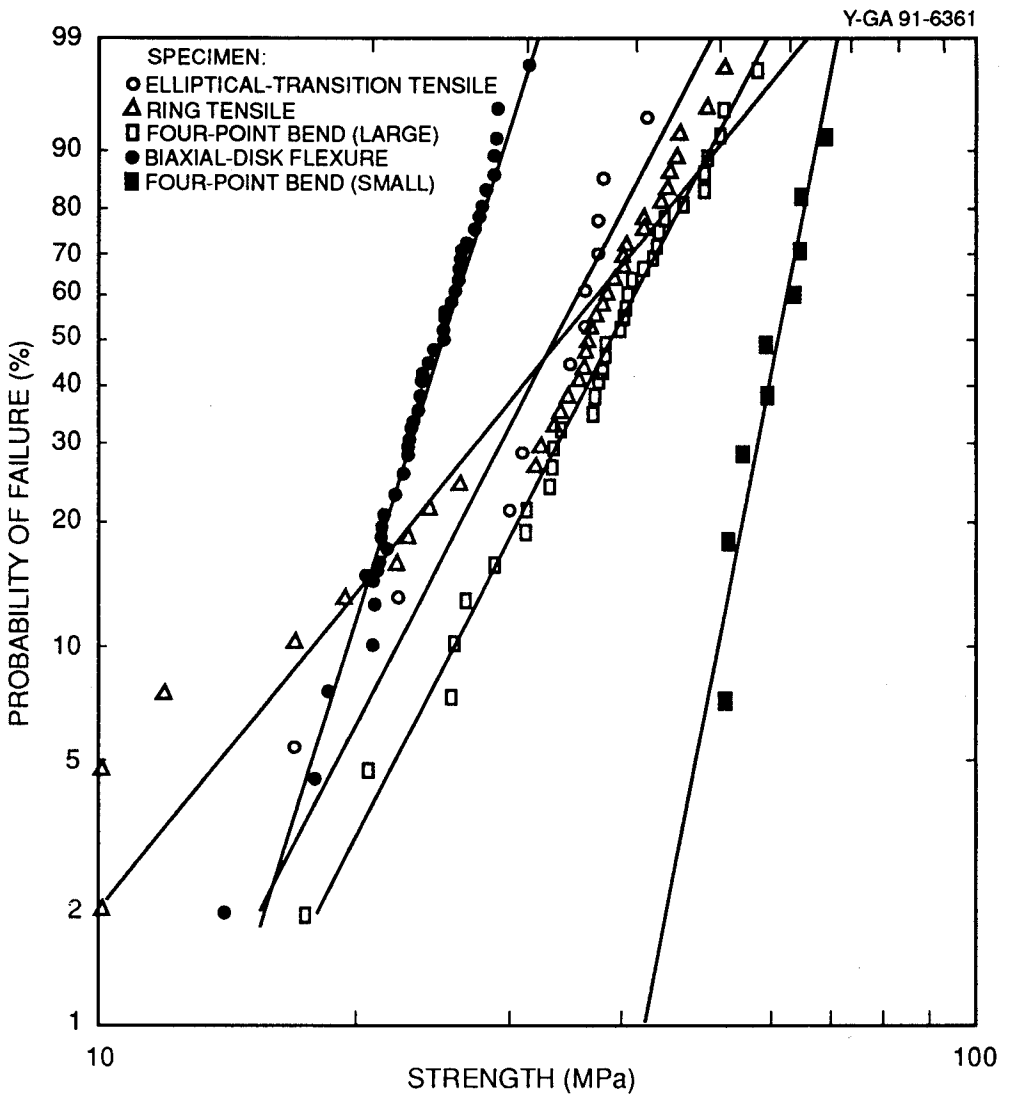

Fig. 1. Composite lithium hydride strength distributions from axially loaded (elliptical-transition) tensile specimens, hydraulically pressurized ring tensile specimens, four-point-flexure specimens, and concentric-ring biaxial-disk-flexure specimens.

The *effective* volume V_E or *effective* area A_E, the parameters required for quantifying size and loading effects on strength, are

$$V_E = \frac{B_V}{(\sigma_b / \sigma_0)^m}$$

and

$$A_E = \frac{B_A}{(\sigma_b / \sigma_0)^m} \quad ,$$

where σ_b is the strength value reported for a test. Once V_E or A_E has been evaluated for each specimen type, strength distributions from differing specimen types or sizes can be compared by using[3]

$$\frac{\sigma_{0,A}}{\sigma_{0,B}} = \left(\frac{V_{E,B}}{V_{E,A}}\right)^{\frac{1}{m}} \tag{3}$$

or

$$\frac{\sigma_{0,A}}{\sigma_{0,B}} = \left(\frac{A_{E,B}}{A_{E,A}}\right)^{\frac{1}{m}} \quad , \tag{4}$$

where subscripts A and B refer to the type or size specimens for which results are to be compared. Use of Eqs. (3) and (4) requires equal m values for each distribution being compared, further implying equal flaw populations in all specimens.

Ideally, similar methods can be used to predict the strength distributions for *components* for which specimen data exist, again requiring identical flaw populations in each. Finite-element-analysis programs would be used to perform the stress analysis and to evaluate the necessary volume and surface integrations. Most complex components, however, are multiaxially stressed, requiring more advanced methodology than the two-parameter Weibull statistical-distribution function. Such methodology is currently receiving considerable attention, but no consensus has been reached on a method for handling multiaxial-stress-state effects.

TENSILE STRENGTH DISTRIBUTIONS OF LITHIUM HYDRIDE

MATERIAL DESCRIPTION

The material from which all test specimens were machined was produced by a warm-pressing method from powders having a broad particle size distribution, ranging from course powders >1000 μm to fine, submicron particles. The powders were produced by grinding cast billets. Thus, each particle is a single crystal, and the grain size distribution of the prepressed material corresponds to the particle size distribution of the starting powder. The temperatures employed in the subsequent warm-press operation were not high enough to allow grain growth, so the final material grain size corresponds to the starting powder distribution.

SPECIMEN DESCRIPTIONS

Four-Point-Flexure Specimen

The one-fourth-point, four-point-flexure test is the preferred test in U.S. Army Military Standard MIL-STD-1942(MR) for ambient-temperature strength testing of ceramic materials.[4] The reported strength is the outer-fiber stress calculated from

$$\sigma_{b,4Pt} = \frac{3PL}{4bh^2} ,$$

where P is the break load. The remaining variables, along with the outer-fiber tensile stress distribution and dimensions, for both size specimens are defined in Fig. 2.

Weil and Daniel[5] have shown that the effective volume and area for this specimen are

$$V_{E,4Pt} = \frac{Lbh(m + 2)}{4(m + 1)^2} \tag{5}$$

and

$$A_{E,4Pt} = L\left(\frac{h}{m + 1} + b\right) \frac{m + 2}{2(m + 1)} . \tag{6}$$

Both Eqs. (5) and (6) account for all tensile-stressed volumes and areas of the specimen that lie within the outer specimen supports.

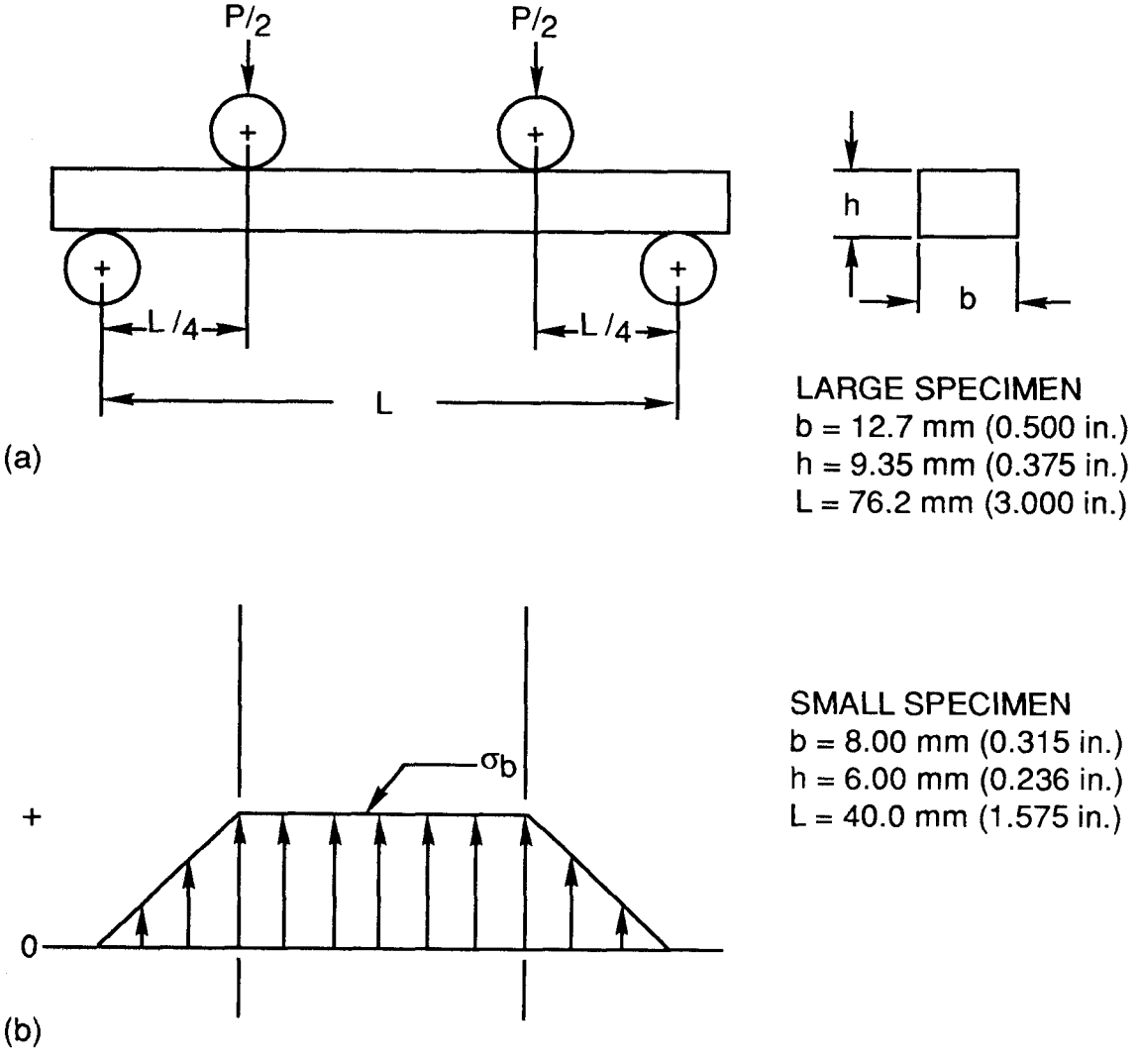

Fig. 2. Four-point-flexure (a) specimen geometry and (b) outer-fiber stress profile.

Ring Tensile Specimen

The ring tensile test, introduced by Sedlacek and Halden,[6] consists of a thick-wall cylinder internally pressurized to failure. A thin, rubber bladder separates the hydraulic fluid from the specimen, and fixturing is designed to absorb all axial load. A circumferentially uniform hoop stress that decreases in value with increasing radius according to a^2/r^2 is generated in the wall as shown in Fig. 3. The reported strength is the maximum inner-wall tensile stress calculated from the thick-wall equation

$$\sigma_{b,Ring} = P \frac{b^2 + a^2}{b^2 - a^2},$$

where P is the pressure at failure and the remaining variables are defined in Fig. 3. A compressive component of stress is also present on the inner surface equal in magnitude to the pressure and decreasing to zero at the outer surface.

The effective volume and effective area for this specimen, derived in Appendix A, are

$$V_{E,Ring} = 2\pi h a^{2m} \frac{b^{2-2m} - a^{2-2m}}{2 - 2m},$$

which includes the entire specimen volume, and

$$A_{E,Ring} = 2\pi \left[ah + \frac{a^2 h}{b} + \frac{1}{1 - m} \left(\frac{a^{2m}}{b^{2m-2}} - a^2 \right) \right],$$

which includes both inner and outer surfaces and both ends. The compressive stress component is not considered to contribute to fracture in either derivation.

Elliptical-Transition Tensile Specimen

The elliptical-transition tensile specimen is a pure uniaxial tensile specimen with a straight cylindrical gage section, length L and diameter d, and elliptical-transition regions that terminate in button-head gripping ends. This specimen is shown in Fig. 4, along with the idealized axial-stress distribution. When this specimen was tested in the hydraulically operated, self-aligning grip system developed at the Oak Ridge National Laboratory,[7] measured bending strains in the gage section were less than 1%. Finite-element analysis of the elliptical-transition tensile specimen shows no significant stress concentrations in the transition region. The reported strength is

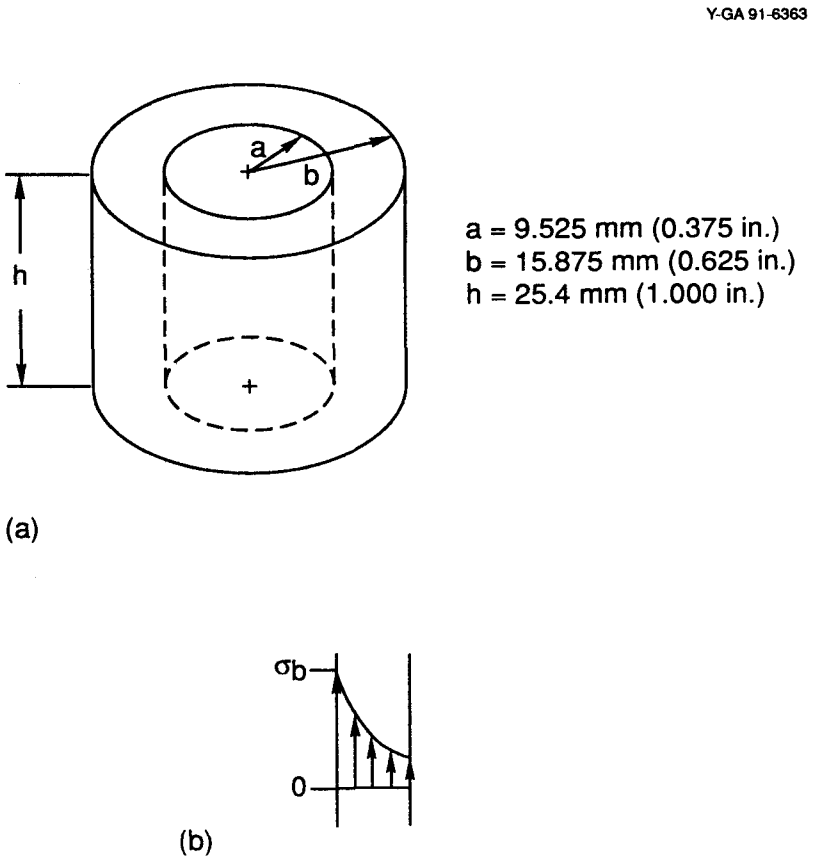

Fig. 3. Ring tensile (a) specimen geometry and (b) through-wall circumferential stress profile. Axial stress is zero.

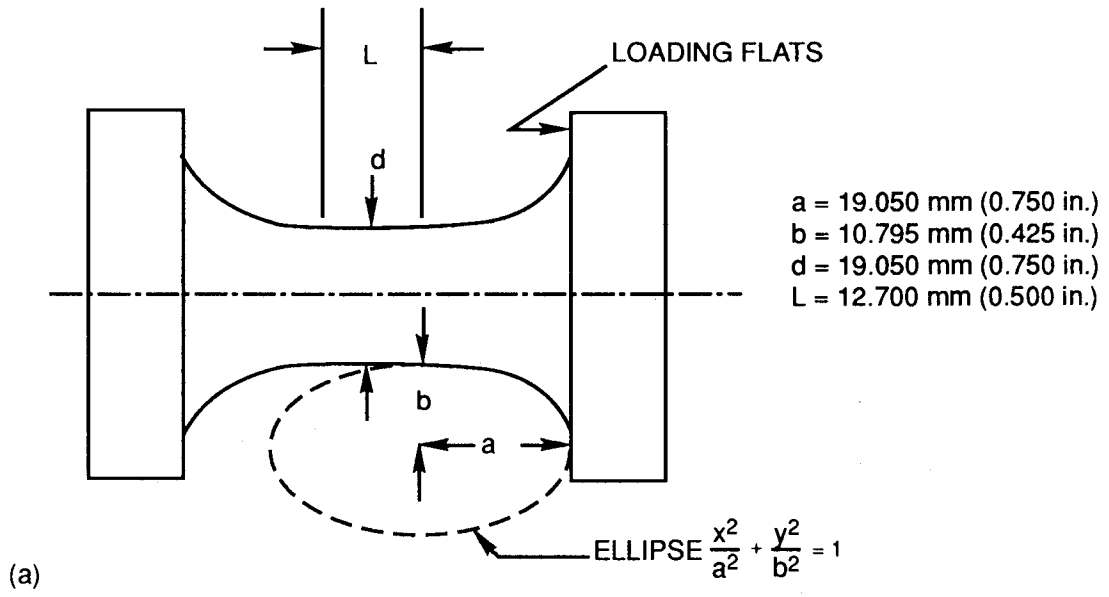

(a)

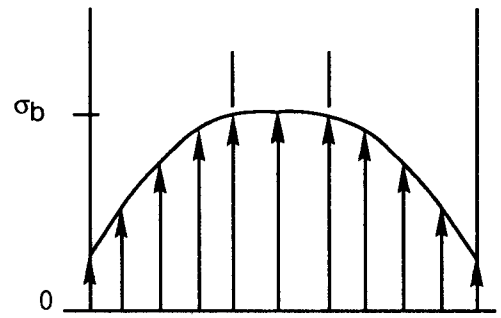

(b)

Fig. 4. Elliptical-transition tensile (a) specimen geometry and (b) axial stress profile in the gage and transition regions.

$$\sigma_{b,ETT} = \frac{4P}{\pi d^2} ,$$

where P is the fracture load, d is the cylindrical-gage-section diameter, and ETT is the elliptical-transition tensile specimen. This minimum diameter is used whether the fracture occurred inside or outside the gage section.

The effective volume and effective area for the elliptical-transition tensile specimen, derived in Appendix B, are

$$V_{E,ETT} = \frac{\pi d^2 L}{4} + \frac{\pi d^{2m}}{2} \int_{x=0}^{a} \left[d + 2b \left(1 - \sqrt{1 - \frac{x^2}{a^2}} \right) \right]^{2-2m} dx \tag{7}$$

and

$$A_{E,ETT} = \pi dL + 2\pi d^{2m} \int_{x=0}^{a} \left[d + 2b \left(1 - \sqrt{1 - \frac{x^2}{a^2}} \right) \right]^{1-2m} dx , \tag{8}$$

with the variables defined in Fig. 4. Both $V_{E,ETT}$ and $A_{E,ETT}$ are expressed as integrals that are evaluated numerically by using a Gaussian technique.[8] For the specimen dimensions of Fig. 4, both Eqs. (7) and (8) are evaluated as a function of the Weibull modulus, m, in Fig. 5.

Note that, in Fig. 5, m values below about 10 drastically increase both $V_{E,ETT}$ and $A_{E,ETT}$. This is true for all specimens. Consequently, there is an increased risk of failure in lower-stress regions outside the gage section, with the greater flaw density associated with low m values.

Biaxial-Disk-Flexure Specimen

A variety of biaxial-disk-flexure tests are found in the literature. These range from the application of a uniform pressure on a ring-supported disk[9] to the biaxial equivalent of the three-point-bend test wherein a single-point load is applied at the center of a ring-supported disk.[10,11] The concentric-ring biaxial-disk-flexure test[12-14] used in this work is the biaxial equivalent of the four-point-bend test.

As shown in Fig. 6, load is applied uniformly to the concentric rings, creating a through-thickness-varying uniform equibiaxial stress state within the inner ring. As is also shown, the radial and tangential stresses differ considerably between the inner and the outer ring.

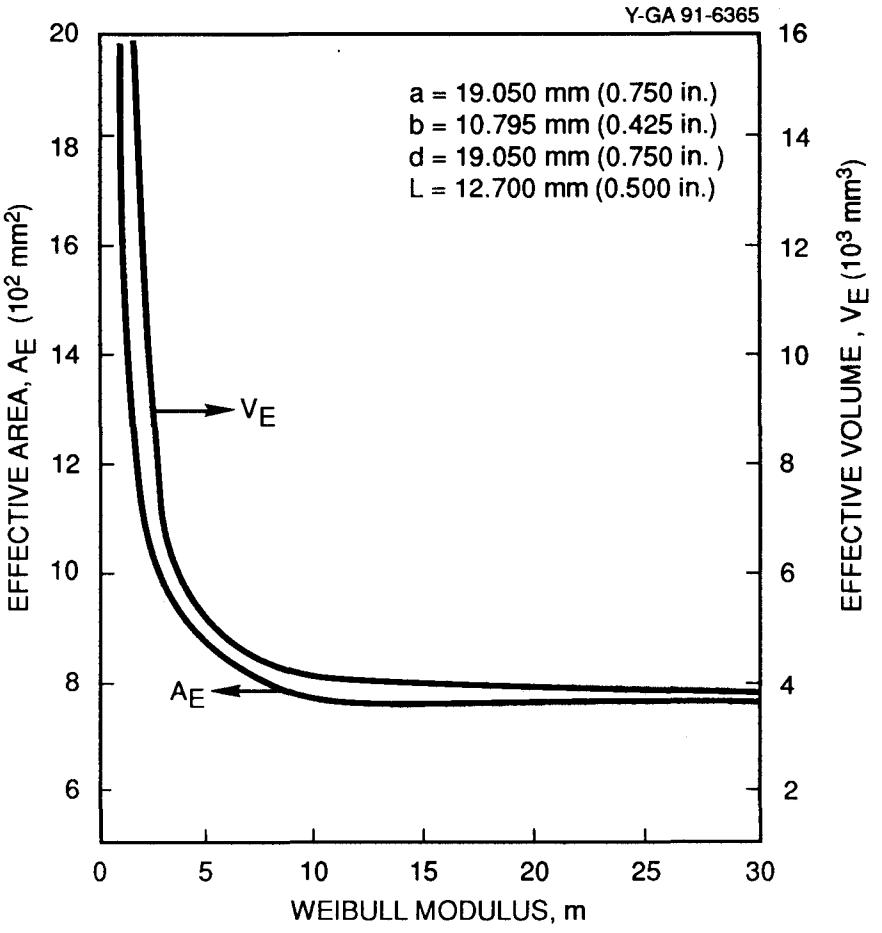

Fig. 5. Effective area and effective volume [Eqs. (7) and (8)] evaluated for the elliptical-transition tensile specimen of Fig. 4 as a function of Weibull modulus.

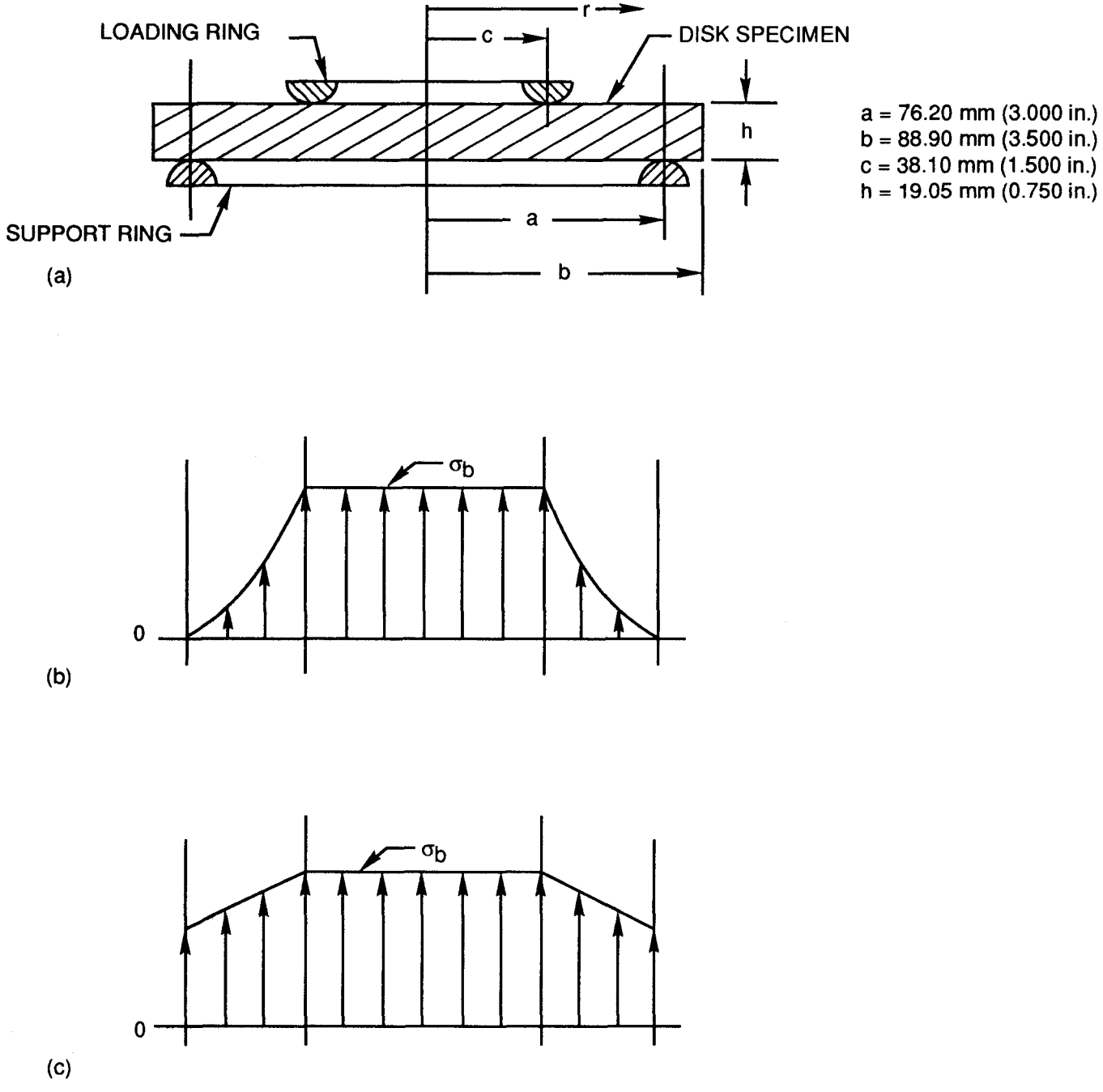

Fig. 6. Biaxial-disk-flexure specimen geometry and outer-fiber stress profiles. (a) Disk specimen geometry; (b) tensile surface radial-stress profile; and (c) tensile surface tangential-stress profile.

The reported strength is the maximum outer-fiber stress calculated from[12]

$$\sigma_{b,BDF} = \frac{3P}{2\pi h^2}\left[(1 - \nu)\,\frac{a^2 - c^2}{2a^2}\,\frac{a^2}{b^2} + (1 + \nu)\ln\left(\frac{a}{c}\right)\right],$$

where P is the load at fracture, ν is the Poisson ratio (0.08), *BDF* is the biaxial-disk-flexure specimen, and the remaining variables are shown in Fig. 6.

Polyaxial stresses existing in this test specimen present problems for Weibull statistics, which are purely mathematical models lacking in physical meaning. Considerable effort is being exerted to develop more realistic approaches, such as probabilistic fracture mechanics, but this effort is still in its infancy. In the derivations of the equivalent volume and area equations for the biaxial-disk specimen (Appendix C), Weibull theory assumes that only the normal stress acting on the flaw face contributes to failure.[14] Between the inner and the outer ring, this normal stress is assumed to be the larger tangential stress. The effective volume and area derived by using simple Weibull relationships for the biaxial-disk-flexure specimen are

$$V_{E,BDF} = \frac{\pi h c^2}{2(m+1)} + 2\pi\left(\frac{1 - \nu^2}{aL_9}\right)^m \frac{h}{2(m + 1)}\int_{r=c}^{a}\left\{\frac{aL_9}{1 + \nu} - r\,G_6(r) + \frac{h^2\nu}{6aL_9}\left[aL_9 - r\,G_9(r)\right]\right\}^m 2r\,dr \quad (9)$$

and

$$A_{E,BDF} = \pi c^2 + \frac{2\pi}{a^m L_9^m}\int_{r=c}^{a}\left\{aL_9(1 - \nu) - r\,G_6(r)\,(1 - \nu^2) + \frac{h^2\nu}{6}\left[L_9 - r\,G_9(r)\right]\right\}^m r\,dr, \quad (10)$$

where L_9 is Roark and Young's plate constant,[15]

$$L_9 = \frac{c}{a}\left\{\frac{1 + \nu}{2}\ln\frac{a}{c} + \frac{1 - \nu}{4}\left[1 - \left(\frac{c}{a}\right)^2\right]\right\},$$

and $G_6(r)$ and $G_9(r)$ are variable functions[15] of the radius, r, defined as

$$G_6(r) = \frac{c}{4r}\left[\left(\frac{c}{r}\right)^2 - 1 + 2\ln\frac{r}{c}\right]$$

and

$$G_9(r) = \frac{c}{r}\left\{\frac{1+\nu}{2}\ln\frac{r}{c} + \frac{1-\nu}{4}\left[1-\left(\frac{c}{r}\right)^2\right]\right\}.$$

Equations (9) and (10) are evaluated in Fig. 7 over a typical range of Weibull modulus, m, for ceramic materials and the specimen size of Fig. 6. Again, both A_E and V_E are highly dependent upon m.

EXPERIMENTAL RESULTS, ANALYSIS, AND DISCUSSION

Strengths from the five different specimens are tabulated in Appendix D and plotted in Weibull coordinates in Fig. 1. In Fig. 1, the superimposed straight lines are linear least-squares fits to the data. Nonlinearity is prevalent in both the large four-point-bend and the ring tensile distributions and is noted to a lesser extent in the lower portion of the other distributions. Also, there are major differences in the slopes of the distributions. These nonlinearities and inconsistent m values suggest that two or more flaw populations contribute to the failure process. Since two-parameter Weibull statistics are based on linear distributions, each data set was separated into upper and lower data sets by using the censored-data method of Johnson.[16,17]

Low-strength points in the large four-point-bend specimen data were censored, and the remaining points were reranked and replotted. This process was repeated until the upper distribution appeared linear and m was defined for this specimen distribution. The remaining specimen data sets were likewise censored until each upper distribution attained m values similar to the reference large four-point-bend m value. All points censored from the upper distribution make up the lower distribution.

The resulting upper distributions (Fig. 8) now meet the requirement of near-equal m values for the application of Eqs. (3) and (4). Considerable differences remain in m of the lower distributions (Fig. 9), and the nonlinearity in the ring tensile lower distribution indicates that more than two flaw distributions are likely present in the overall data set for this specimen. An analysis was not performed on either the elliptical-transition tensile specimen lower suspensions (which contained only two points) or the small four-point-bend specimen (which exhibited no surface-related failures). The variations in m for the lower data distributions can be attributed, at least partially, to the low number of data points.

Fractography on four elliptical-transition tensile specimens verifies the association of high-strength failures with volumetric-related-fracture initiation sites and low-strength failures with surface-fracture initiation sites. The two highest-strength and the two lowest-strength elliptical-transition tensile specimen surface-fracture initiation sites (Fig. 10) correlate with the assumed relationship.

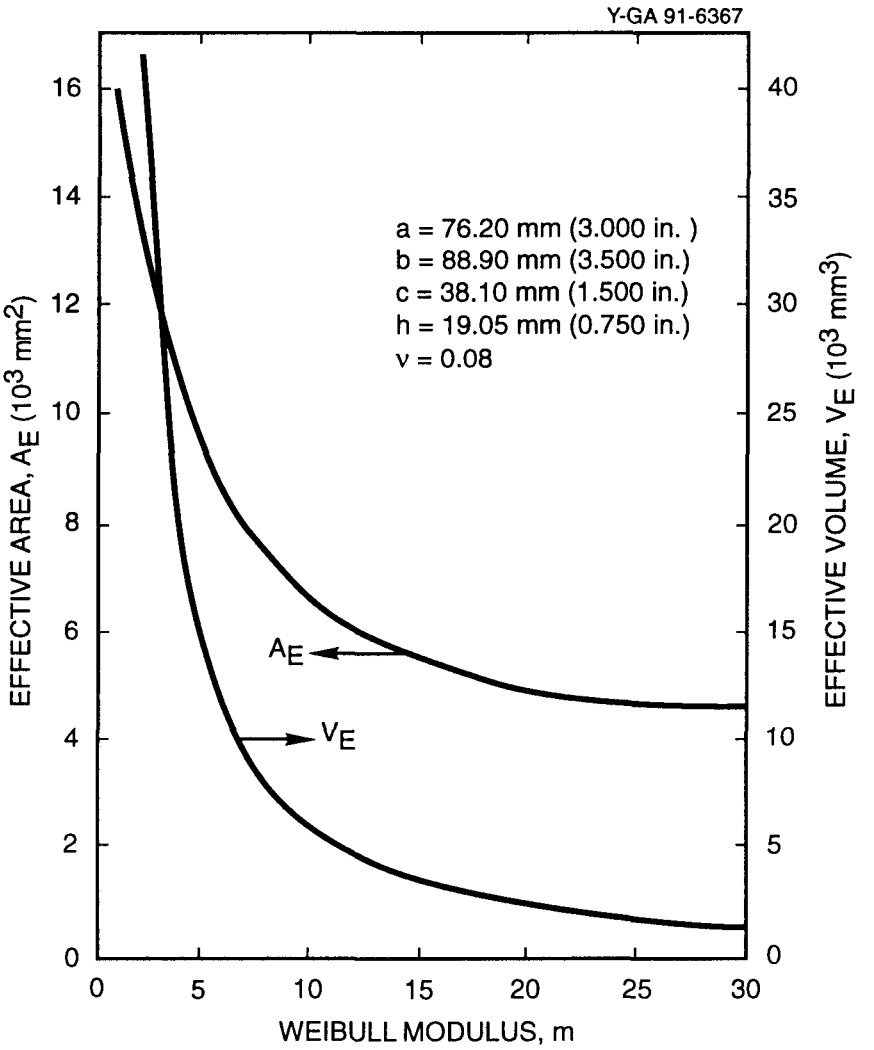

Fig. 7. Effective area and effective volume [Eqs. (9) and (10)] evaluated for the biaxial-disk-flexure specimen of Fig. 6 as a function of Weibull modulus.

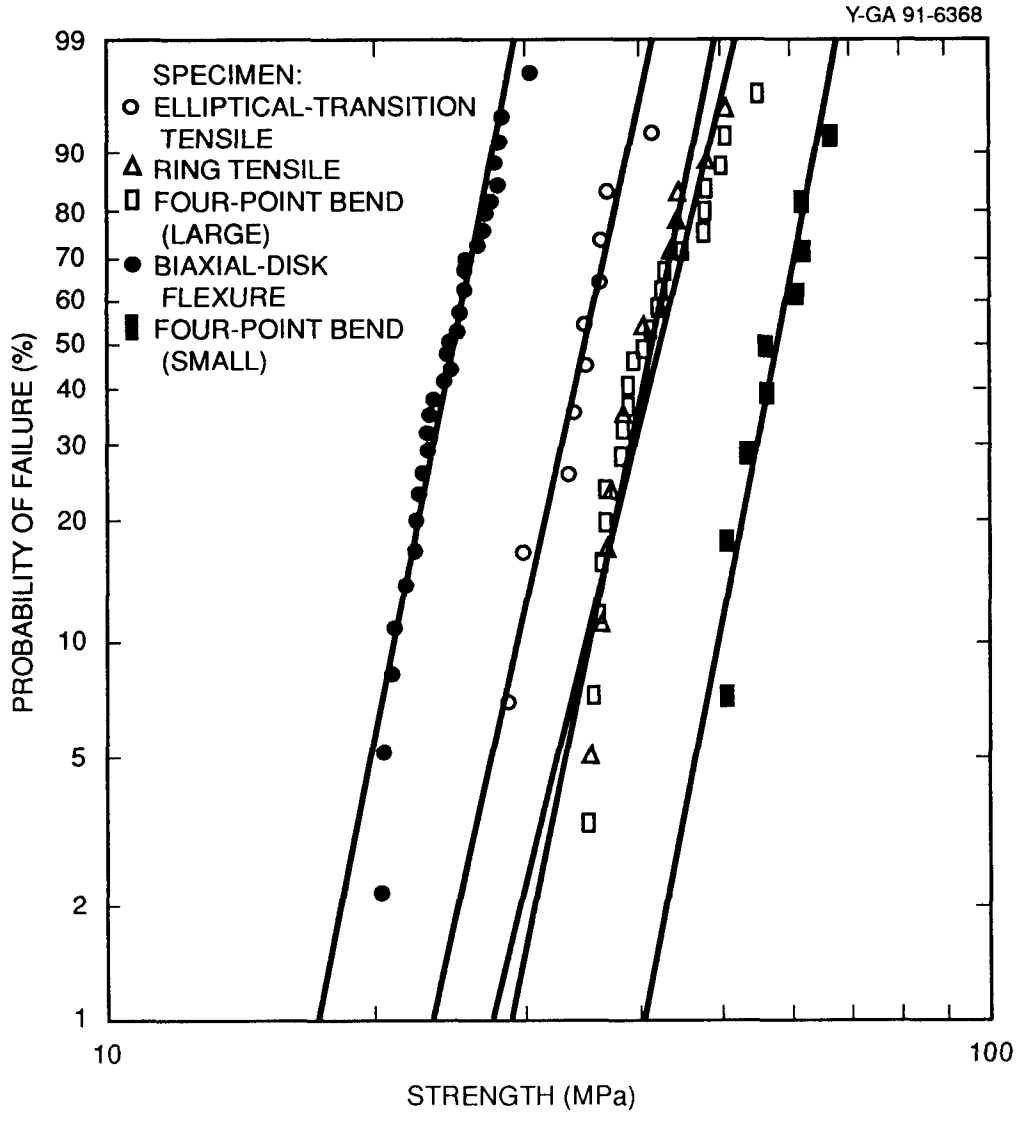

Fig. 8. Composite lithium hydride strength distributions of upper suspensions from four tensile specimen types.

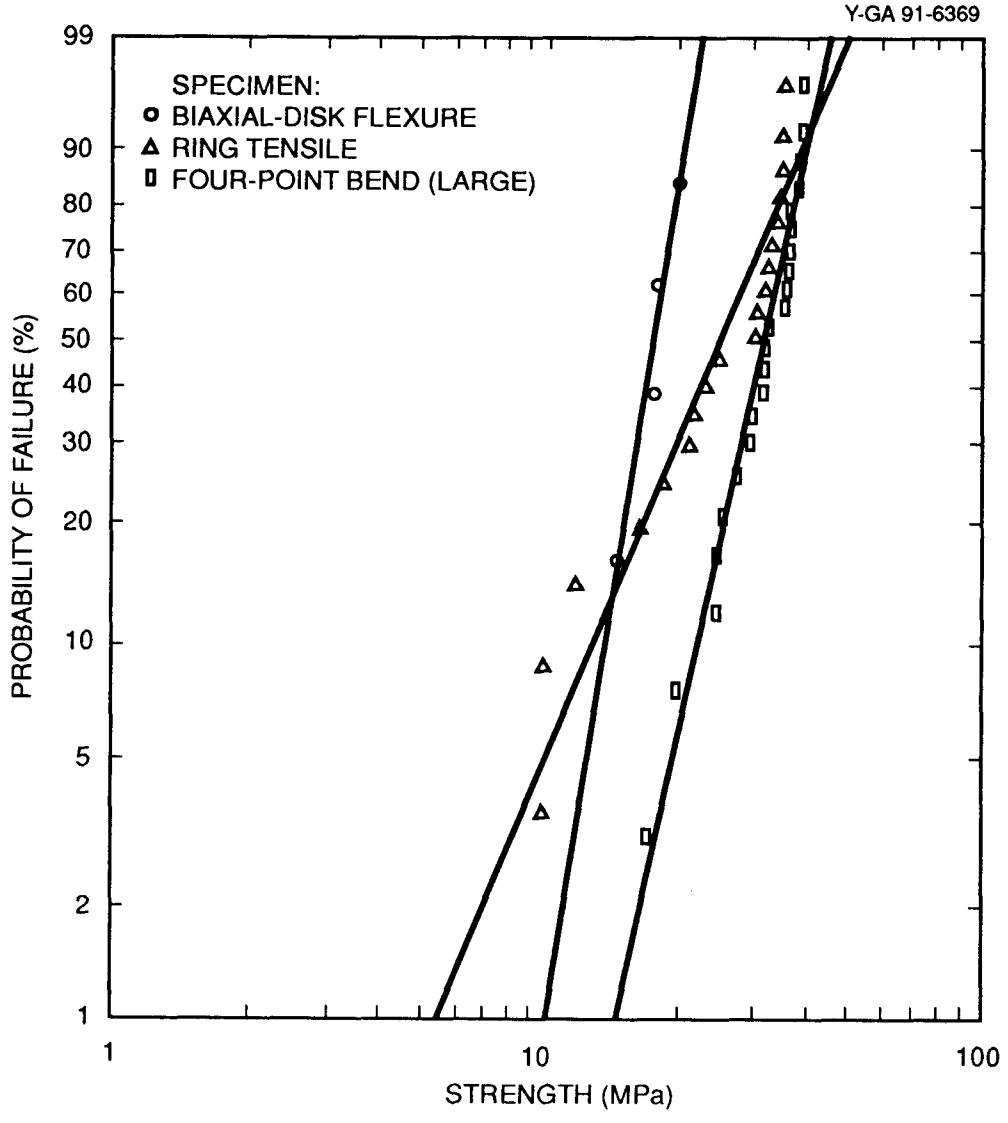

Fig. 9. Composite lithium hydride strength distributions of lower suspensions from three tensile specimen types. Both the ring tensile data and the four-point-bend data remain nonlinear, an indication that multiple-flaw populations are still present.

(a)

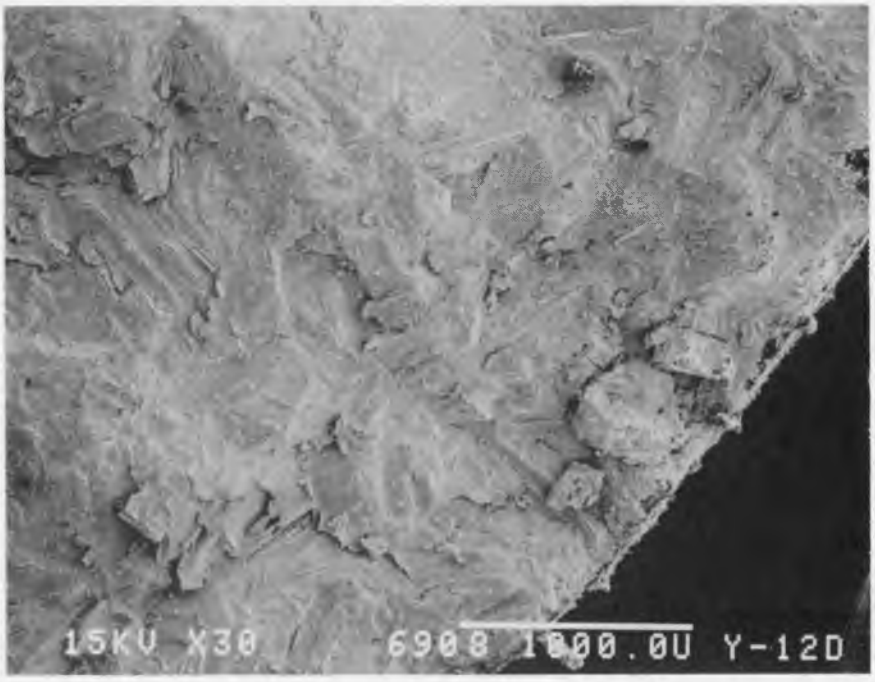

(b)

Fig. 10. Fracture surfaces of two lowest-strength and two highest-strength elliptical-transition tensile specimens, which confirm the association of low-strength failures with surface flaws and high-strength failures with volumetric flaws. (a) Surface-fracture initiation site at 16.9 MPa; (b) surface-fracture initiation site at 21.9 MPa; (c) internal-fracture initiation site at 36.9 MPa; and (d) internal-fracture initiation site at 41.3 MPa.

(c)

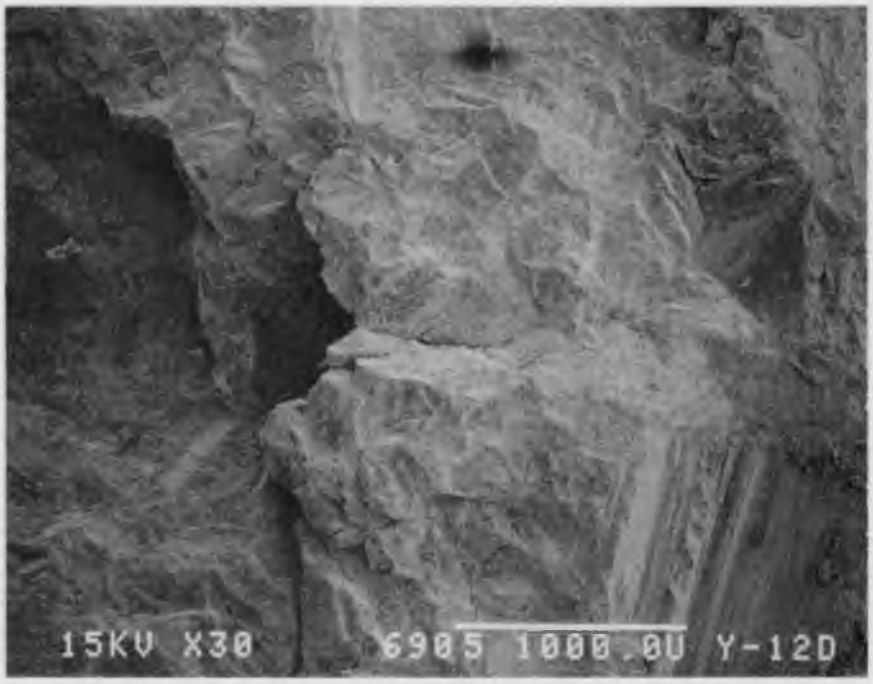

(d)

Fig. 10 (continued)

Table 1 lists Weibull parameters m and σ_0, the coefficient of determination r^2 for the data fit, the effective volumes and areas for each specimen type (with m = 11.8 and 5.5 from the large four-point-bend reference distributions), and the number of total and censored points in each set. These values and Eqs. (3) and (4) will now be used to quantify size effects on strength distributions from the five different specimens.

As shown by Quinn,[3] a log-log plot of σ_0 vs V_E or A_E of Eqs. (3) and (4) with a slope of $-1/m$, when plotted through the reference large four-point-bend data, should fit the results of the other specimens if the two-parameter Weibull theory adequately models size effects. The upper-suspension characteristic strength values from the ring tensile and elliptical-transition tensile specimens are in excellent agreement with the effective volume theory (Fig. 11), whereas σ_0 for the small four-point-flexure tests is slightly above the theoretical value. The characteristic strength for the biaxial-disk-flexure tests is well below the Weibull prediction.

The lower-suspension-data characteristic strengths (Fig.12) are not as well defined by the effective area theory, because only two uniaxial-specimen-type data sets contained enough lower-suspension points to generate Weibull plots. The quantity σ_0 for the biaxial disk is low, as expected, because of biaxial effects. Whereas the ring tensile σ_0 fits the predicted value, the nonlinearity in the ring tensile lower distribution (Fig. 9) indicates multiple-flaw distributions, thus invalidating use of the two-parameter Weibull function. Also, the ring tensile m value is much lower than the reference value (Table 1), violating the assumptions of Eq. (4).

Surface flaws can generally be traced to machining damage, and machining methods differed for each specimen type. Both the elliptical-transition tensile and the disk-flexure specimen surfaces are single-point machined in a lathe, all surfaces of the four-point-bend specimens are milled, and the ring tensile fabrication consists of both deep, uncooled core drilling and final lathe finishing. Dye-penetrant studies on the ring tensile specimen have shown significant cracks remaining on finish-machined, cored surfaces, probably thermally generated during the coring process. These machining differences probably account for both the different lower-strength-distribution m values in Table 1 and the multiple-flaw distributions in the ring tensile lower-strength distribution (Fig. 9).

The trend in effective area strength prediction (Fig. 12) is correct, but m differences and nonlinearity in the ring tensile data (both related to machining differences), combined with the absence of elliptical-transition and small four-point-bend results, do not adequately prove the quantitative relationship between effective area and the characteristic strengths for the lower distributions.

Identical flaw populations are assumed when Weibull scaling is applied. Volumetric populations, which consist predominantly of grains, meet this requirement, whereas the variations in machined surfaces do not.

Table 1. Weibull parameters for lithium hydride from the four specimen types after separation into upper and lower distributions

Specimen type	Weibull modulus, m (dimensionless)	Characteristic strength, σ_0 (MPa)	Coefficient of determination, r^2 (0–1.0)	Number of points	Effective volume, V_E (mm^3)	Effective area, A_E (mm^2)
Upper distribution:						
Four-point flexure (large)	11.8	47.8	0.903	13 of 35	194[a]	
Four-point-flexure (small)	13.0	60.0	0.911	9 of 9	39[a]	
Ring tensile	12.2	43.3	0.877	16 of 35	670[a]	
Elliptical-transition tensile	11.3	36.3	0.927	10 of 12	4085[a]	
Biaxial-disk flexure	12.9	25.8	0.935	32 of 36	4546[a]	
Lower distribution:						
Four-point flexure (large)	5.5	35.0	0.958	22 of 35		623[b]
Four-point flexure (small)	*c*	*c*	*c*	0 of 9		202[b]
Ring tensile	2.8	29.6	0.919	19 of 35		2557[b]
Elliptical-transition tensile	*c*	*c*	*c*	2 of 12		858[b]
Biaxial-disk flexure	7.6	18.9	0.942	4 of 36		9032[b]

[a] Weibull modulus m = 11.8 from large four-point bend used as upper distribution reference.
[b] Weibull modulus m = 5.5 from large four-point bend used as lower distribution reference.
[c] Inadequate data for Weibull analysis.

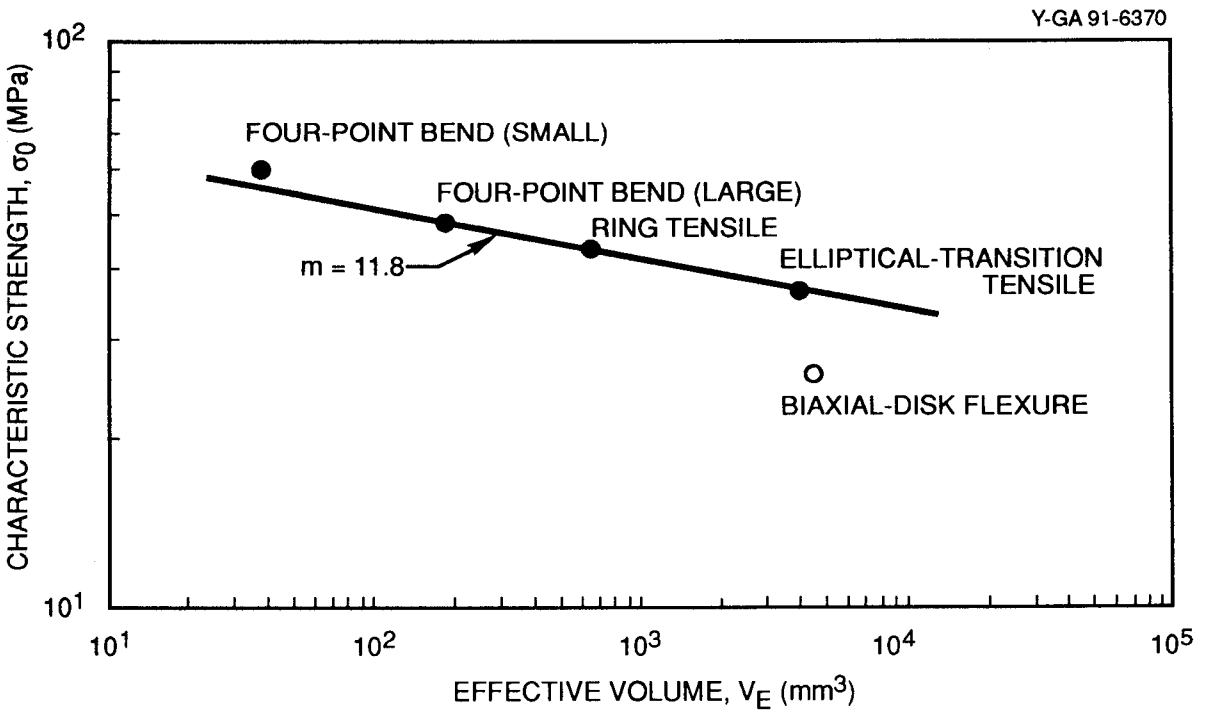

Fig. 11. Effect of effective volume on characteristic strength for the upper-suspension lithium hydride data. The solid line represents the theoretical relation, and points are experimental values.

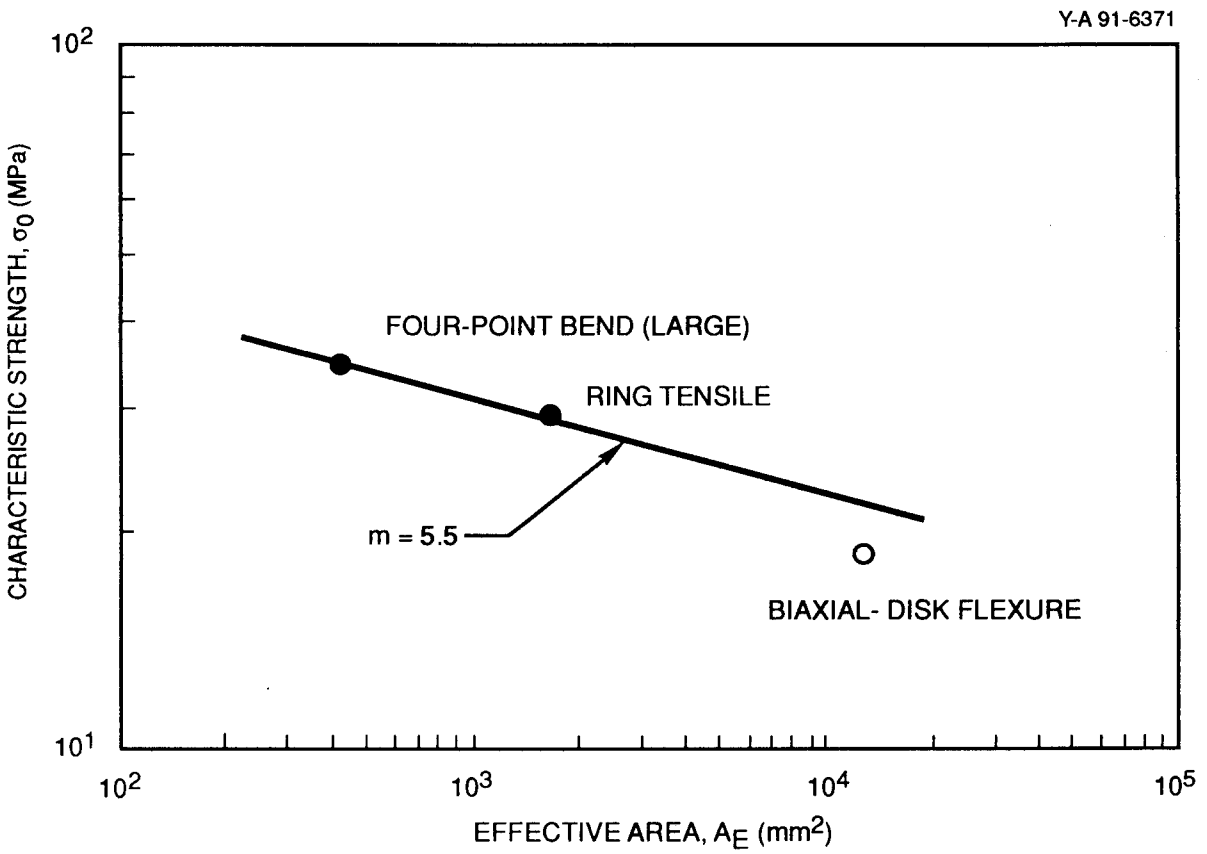

Fig. 12. Effect of effective specimen surface area on characteristic strength for the lower-suspension lithium hydride data. The solid line represents the theoretical relation, and points are experimental values.

CONCLUSIONS AND RECOMMENDATIONS

Different uniaxial tensile-strength distributions for different sizes and types of lithium hydride specimens are quantitatively explained by using the effective volume and, to a lesser degree, effective area concepts in conjunction with the Weibull two-parameter, statistical-distribution function. High-strength fractures are associated both theoretically and experimentally with internal-fracture initiation sites by using effective volume theory and fracture-surface analysis to identify fracture initiation locations. Limited numbers of lower-strength fractures and different specimen-machining methods associated with each specimen type prevented the making of definitive conclusions on the applicability of effective area theory to lower-strength fracture data.

The Weibull theory did not satisfactorily predict biaxial-specimen strengths from uniaxial-strength data. It is recommended that alternative theories be investigated for a solution to this problem. Since most components would experience multiaxial stresses, scaling from uniaxial-specimen data to component sizes can now be done only for simple stress states.

ACKNOWLEDGMENTS

The author wishes to express his gratitude to the following individuals: D. A. Waldrop, who set up and conducted most of the tests; R. Baylor, Jr., for material, specimens, and text review; C. M. Davenport for assistance in equation integrations; and W. L. Bolinger for the scanning electron microscopy fracture-surface examinations.

REFERENCES

1. W. Weibull, "Statistical Theory of Strength of Materials," *Ing. Vetenskaps Akad. Handl.* **151**, 1–45 (1939); *Ceram. Abstr.* **19**(3), 78 (1940).

2. W. Weibull, "Statistical Distribution Function of Wide Applicability," *J. Appl. Mech.* **18**(3), 293–97 (1951).

3. G. D. Quinn, *Flexure Strength of Advanced Ceramics — A Round Robin Exercise*, MIL TR 89-62, United States Army Materials Technology Laboratory, Watertown, Massachusetts, July 1989.

4. Department of the Army, Washington, D.C., *Flexural Strength of High Performance Ceramics at Ambient Temperature*, United States Army Military Standard, MIL-STD-1942(MR), November 1983.

5. N. A. Weil and I. M. Daniel, "Analysis of Fracture Probabilities in Nonuniformly Stressed Brittle Materials," *J. Am. Ceram. Soc.* **47**(6), 268–74 (1964).

6. R. Sedlacek and F. A. Halden, "Method for Tensile Testing of Brittle Materials," *Rev. Sci. Instrum.* **33**(3), 298–300 (1962).

7. K. C. Liu and C. R. Brinkman, "Tensile Cyclic Fatigue of Structural Ceramics," pp. 279–84 in *Proceedings of the Twenty-Third Automotive Technology Development Contractors' Coordinated Meeting*, P-165, Society of Automotive Engineers, Warrendale, Pennsylvania, March 1986.

8. A. Ralston, *A First Course in Numerical Analysis*, McGraw-Hill Book Company, New York, 1965.

9. D. K. Shetty, A. R. Rosenfield, W. H. Duckworth, and P. R. Held, "A Biaxial-Flexure Test for Evaluating Ceramic Strengths," *J. Am. Ceram. Soc.* **66**(1), 36–42 (1983).

10. K. C. Radford and F. F. Lange, "Loading (L) Factors for the Biaxial Flexure Test," *J. Am. Ceram. Soc.* **61**(5-6), 211–13 (1978).

11. R. Kao, N. Perrone, and W. Capps, "Large-Deflection Solution of the Coaxial-Ring Circular-Glass Plate Flexure Problem," *J. Am. Ceram. Soc.* **54**(11), 566–71 (1971).

12. M. N. Giovan and G. Sines, "Biaxial and Uniaxial Data for Statistical Comparisons of a Ceramic's Strength," *J. Am. Ceram. Soc.* **62**(9–10), 510–15 (1979).

13. M. N. Giovan and G. Sines, "Strength of a Ceramic at High Temperature Under Biaxial and Uniaxial Tension," *J. Am. Ceram. Soc.* **64**(2), 68–73 (1981).

14. K. Ikeda and H. Igaki, "Effects of Polyaxial Stress States on Fracture Strength of Soda-Lime Glass," *J. Am. Ceram. Soc.* **70**(7), 470–74 (1987).

15. R. J. Roark and W. C. Young, *Formulas for Stress and Strain*, McGraw-Hill Book Company, New York, 1975.

16. L. G. Johnson, *The Statistical Treatment of Fatigue Experiments*, Elsevier, New York, 1964.

17. R. B. Abernethy, J. E. Breneman, C. H. Medlin, and G. L. Reinman, *Weibull Analysis Handbook*, AFWAL-TR-83-2079, Wright-Patterson Air Force Base, Ohio, 1983.

APPENDIX A

EFFECTIVE VOLUME AND AREA DERIVATIONS FOR THE RING TENSILE SPECIMEN

THE EFFECTIVE VOLUME

For an internally pressurized, thick-walled vessel with open ends and external fixturing reducing axial forces in the cylinder to zero, the principal stress fields are a circumferential tensile component that varies through the wall as

$$\sigma(r) = P\frac{a^2(b^2 + r^2)}{r^2(b^2 - a^2)}$$

and a compressive radial component equaling P, the internal pressure, at the inner radius a and decreasing to zero at the outside radius b. Only the tensile component will be considered as contributing to fracture. The quantity $\sigma(r)$ is redefined in terms of the reported strength σ_b, the maximum tensile stress occurring at the inner surface where $r = a$, as $\sigma(r) = \sigma_b(a^2/r^2)$.

If we use the cylindrical-volume element $dV = 2\pi rh\ dr$ of Fig. A.1, the risk of rupture is

$$B = \int_V \left[\frac{\sigma(r)}{\sigma_0}\right]^m dV = \int_{r=a}^{b} \left[\frac{\sigma_b(a^2/r^2)}{\sigma_0}\right]^m 2\pi rh\ dr\ ,$$

and the effective volume $V_{E,Ring}$ is the risk of rupture divided by the stress function $(\sigma_b/\sigma_0)^m$; thus,

$$V_{E,Ring} = 2\pi h \int_{r=a}^{b} r\left(\frac{a^2}{r^2}\right)^m dr\,, \tag{A.1}$$

which can be integrated either numerically or in closed form as

$$V_{E,Ring} = 2\pi h a^{2m}\ \frac{b^{2-2m} - a^{2-2m}}{2 - 2m}\ . \tag{A.2}$$

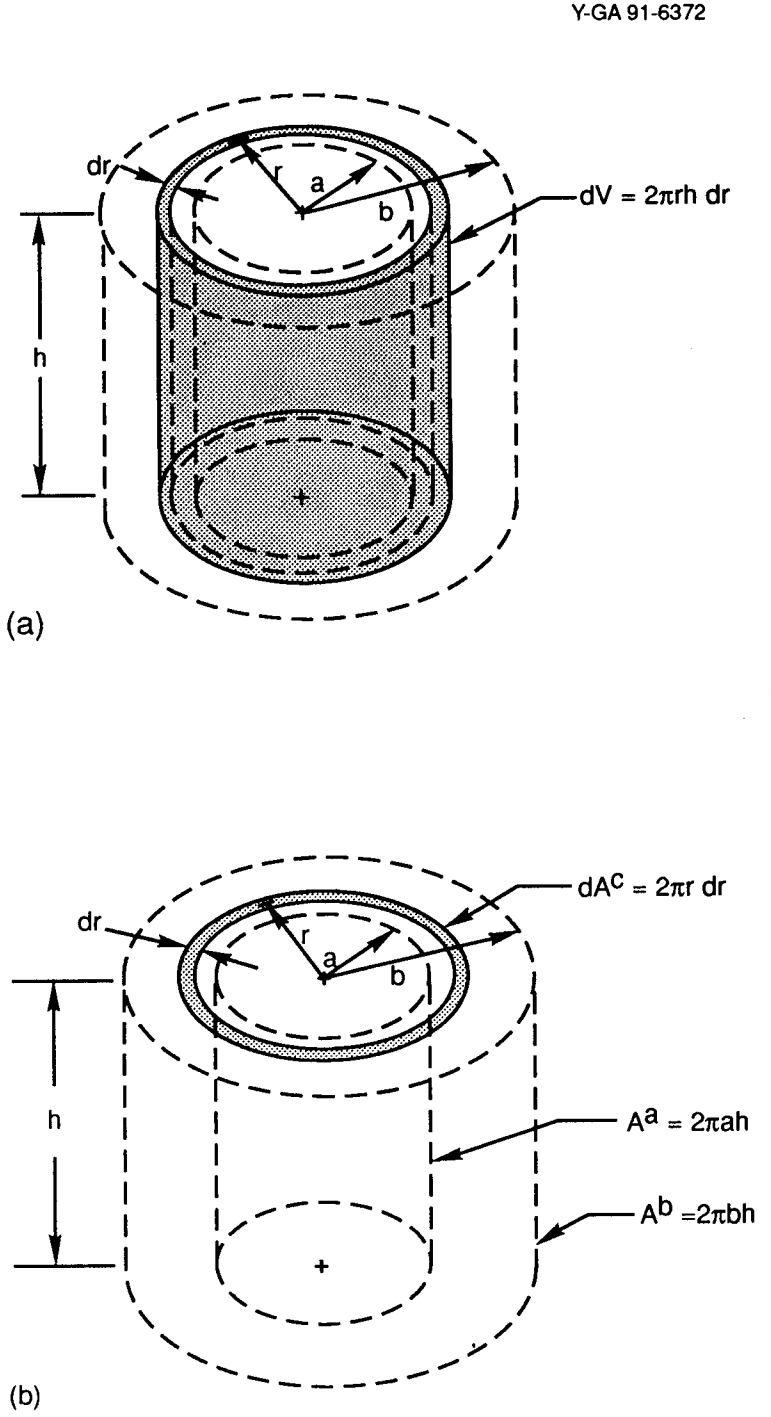

Fig. A.1. Definition of volume and surface elements used to derive effective volume and area for the ring tensile specimen. (a) Cylindrical volume element used for risk-of-rupture integration over the range $r = a$ to b; (b) annular surface element used for risk-of-rupture integration for ends and inner and outer surface areas subjected to uniform stresses.

THE EFFECTIVE AREA

The effective area of the ring tensile specimen, $A_{E,Ring}$, is composed of three distinct regions, the inner surface, the outer surface, and both ends, all subjected to tensile stress. The stress on each in terms of the reported strength σ_b is

$$\sigma^a = \sigma_b \quad (inner\ surface)\ ,$$

$$\sigma^b = \sigma_b(a^2/b^2) \quad (outer\ surface)\ ,$$

and

$$\sigma^c(r) = \sigma_b(a^2/r^2) \quad (each\ end)\ .$$

The effective areas for both the inner and the outer surfaces where the stresses are uniform on all area elements are simply the areas on which the stress acts, or

$$A^a{}_{E,Ring} = 2\pi ah \qquad (inner\ surface)$$

and

$$A^b{}_{E,Ring} = 2\pi a^2 h/b \qquad (outer\ surface)\ .$$

The risk of rupture for the two ends combined, if we use the circular ring element $dA^c = 2\pi r\, dr$ of Fig. A.1, is

$$B^c = \int_{r=a}^{b} \left[\frac{\sigma(r)}{\sigma_0}\right]^m dA^c = 2\int_{r=a}^{b} \left[\frac{\sigma_b(a^2/r^2)}{\sigma_0}\right]^m 2\pi r\, dr\ ,$$

which can be integrated either numerically or in closed form as

$$B^c = \frac{2\pi}{1-m}\left(\frac{\sigma_b}{\sigma_0}\right)^m \left(\frac{a^{2m}}{b^{2m-2}} - a^2\right),$$

which, when divided by the stress function $(\sigma_b/\sigma_0)^m$, becomes the effective area for the two ends combined,

$$A^{c}_{E,Ring} = \frac{2\pi}{1 - m}\left(\frac{a^{2m}}{b^{2m-2}} - a^{2}\right) \quad (two\ ends)\ .$$

The total effective area for the ring tensile specimen, $A_{E,Ring}$, is the sum of the components $A^{a}_{E,Ring}$, $A^{b}_{E,Ring}$, and $A^{c}_{E,Ring}$, which is

$$A_{E,Ring} = 2\pi\left[ah + \frac{a^{2}h}{b} + \frac{1}{1 - m}\left(\frac{a^{2m}}{b^{2m-2}} - a^{2}\right)\right]. \tag{A.3}$$

APPENDIX B

EFFECTIVE VOLUME AND AREA DERIVATIONS FOR THE ELLIPTICAL-TRANSITION TENSILE SPECIMEN

THE EFFECTIVE VOLUME

The effective volume of the elliptical-transition tensile specimen, $V_{E,ETT}$, is composed of two parts, the center gage section (superscript a), where the stress is the reported strength σ_b, or

$$\sigma^a = \sigma_b \quad (\textit{gage section}) ,$$

and the transition regions (superscript b), where the stress in terms of the reported strength decreases with x, the distance from the uniform gage section, as

$$\sigma^b(x) = \frac{d^2\sigma_b}{\left[d + 2b\left(1 - \sqrt{1 - \frac{x^2}{a^2}}\right)\right]^2} \quad (\textit{transition regions}) . \tag{B.1}$$

Variables are shown in Fig. B.1.

Since the stress is uniform in the gage section, the effective volume here simply equals the volume of the gage section,

$$V^a_{E,ETT} = \frac{\pi d^2 L}{4} \quad (\textit{gage section}) .$$

The risk of rupture for the two transition regions combined, if we use the volume element dV^b of Fig. B.1, is

$$B^b = 2\int_V \left[\frac{\sigma(x)}{\sigma_0}\right]^m dV^b = 2\int_{x=0}^{a} \frac{\pi}{4}\left[d + 2b\left(1 - \sqrt{1 - \frac{x^2}{a^2}}\right)\right]^2 dx ,$$

which reduces to

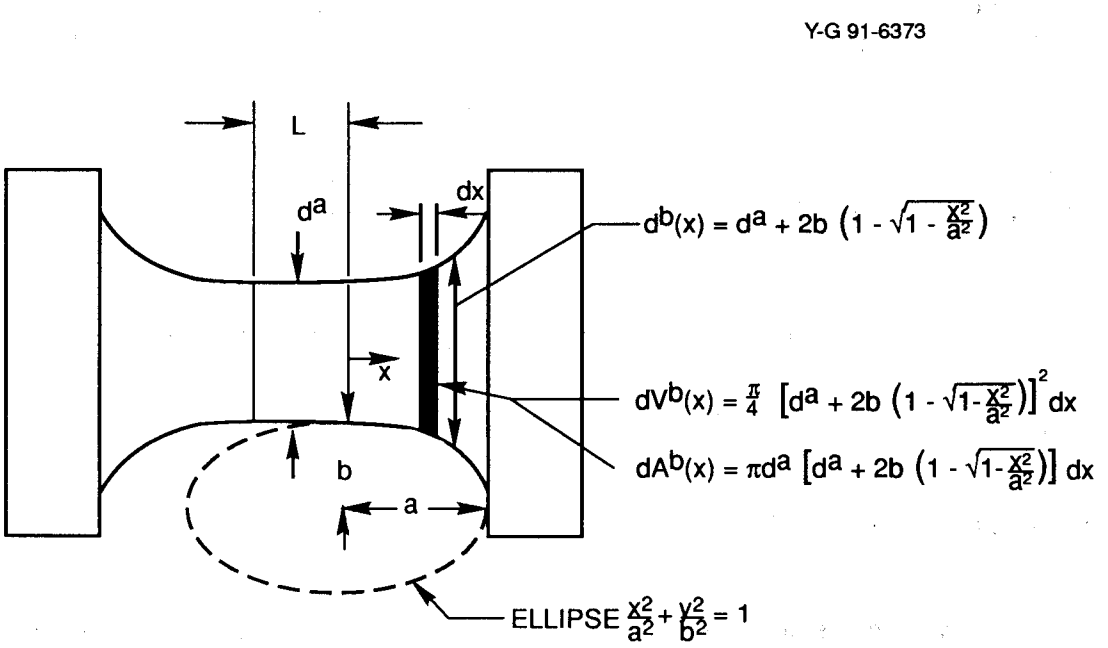

Fig. B.1. Definition of volume and surface elements used to derive effective volume and area for the elliptical-transition tensile specimen.

$$B^b = \frac{\pi}{2} d^{2m} \left(\frac{\sigma_b}{\sigma_0}\right)^m \int_{x=0}^{a} \left[d + 2b\left(1 - \sqrt{1 - \frac{x^2}{a^2}}\right)\right]^{2-2m} dx ,$$

which, after being divided by the stress function $(\sigma_b/\sigma_0)^m$, becomes the effective volume for the combined transition regions,

$$V^b_{E,ETT} = \frac{\pi}{2} d^{2m} \int_{x=0}^{a} \left[d + 2b\left(1 - \sqrt{1 - \frac{x^2}{a^2}}\right)\right]^{2-2m} dx .$$

The total effective volume for the elliptical-transition tensile specimen is the sum of the components $V^a_{E,ETT}$ and $V^b_{E,ETT}$,

$$V_{E,ETT} = \frac{\pi d^2 L}{4} + \frac{\pi d^{2m}}{2} \int_{x=0}^{a} \left[d + 2b\left(1 - \sqrt{1 - \frac{x^2}{a^2}}\right)\right]^{2-2m} dx , \tag{B.2}$$

for which no closed solution could be found, thus requiring numerical-integration methods for evaluation.

THE EFFECTIVE AREA

The effective area of the elliptical-transition tensile specimen, $A_{E,ETT}$, like the effective volume, is composed of two distinct regions, the gage section and the transition region. Again, because the stress on the gage-section surface is everywhere equal to σ_b, the effective area of the gage section equals the surface area of the cylinder,

$$A^a_{E,ETT} = \pi dL \quad \textit{(gage section)}.$$

The surface stress as a function of x in the transition region equals Eq. (B.1), and the area increment shown in Fig. B.1 is

$$dA^{b}_{E,ETT} = \pi\left[d + 2b\left(1 - \sqrt{1 - \frac{x^2}{a^2}}\right)\right]dx \ .$$

The risk of rupture, then, becomes

$$B^{b} = 2\pi\left(\frac{\sigma_b}{\sigma_0}\right)^{m}\int_{x=0}^{a}\left\{\frac{d^2}{\left[d + 2b\left(1 - \sqrt{1 - \frac{x^2}{a^2}}\right)\right]^2}\right\}^{m}\left[d + 2b\left(1 - \sqrt{1 - \frac{x^2}{a^2}}\right)\right]dx \ ,$$

which, when divided by the stress function $(\sigma_b/\sigma_0)^m$ and algebraically reduced, provides the transition region effective area,

$$A^{b}_{E,ETT} = 2\pi\int_{x=0}^{a}\frac{d^{2m}}{\left[d + 2b\left(1 - \sqrt{1 - \frac{x^2}{a^2}}\right)\right]^{2m-1}}dx \qquad (\textit{transition regions}) \ .$$

The total effective area for the elliptical-transition tensile specimen, $A_{E,ETT}$, is the sum of $A^{a}_{E,ETT}$ and $A^{b}_{E,ETT}$, which is

$$A_{E,ETT} = \pi dL + 2\pi d^{2m}\int_{x=0}^{a}\left[d + 2b\left(1 - \sqrt{1 - \frac{x^2}{a^2}}\right)\right]^{2m-1}dx \ , \qquad \text{(B.3)}$$

for which no closed-form solution could be found, thus requiring numerical-integration methods for evaluation.

APPENDIX C

EFFECTIVE VOLUME AND AREA DERIVATIONS FOR THE BIAXIAL-DISK-FLEXURE SPECIMEN

THE EFFECTIVE VOLUME

The effective volume of the biaxial-disk-flexure specimen, $V_{E,BDF}$, is derived in two parts, the region within the inner loading ring (superscript a) and the region between the inner and the outer loading ring (superscript b). Within the inner ring, the equibiaxial stress in terms of the reported strength σ_b varies linearly through the thickness as

$$\sigma^a(y) = \frac{2y}{h}\sigma_b \quad (\textit{central region, } r < c) \ .$$

Since the two-parameter Weibull function is incapable of incorporating multiaxial stresses, the biaxial effects on failure strength are ignored. With the circular-disk-volume element $dV^a = \pi c^2$ of Fig. C.1, the risk of rupture for the central region is

$$B^a = \int_V \frac{\sigma(y)}{\sigma_0}\, dV^a = \int_{y=0}^{h/2} \left(\frac{2\,\frac{y}{h}\,\sigma_b}{\sigma_0} \right)^m \pi c^2 dy \ ,$$

which, when integrated and divided by the stress function $(\sigma_b/\sigma_0)^m$, becomes the effective volume for the central region,

$$V^a_{E,BDF} = \frac{\pi h c^2}{2(m+1)} \quad (\textit{central region, } r < c) \ . \tag{C.1}$$

Outside the central region, the tangential stresses σ_t^b are greater than the radial and, since the larger stresses contribute more to failure and only one can be incorporated into the Weibull model, the tangential stress component will be used exclusively in developing the effective volume and area for the outer region. If we use Roark and Young's relationships for a simply supported, solid, circular plate with a uniform annular line load,[1] the tangential stress $\sigma(r,y)$ in terms of the reported strength value σ_b can be shown to equal

$$\sigma_t^b(r,y) = 2\,\frac{y}{h}\,\frac{1-\nu^2}{aL_9}\left(\sigma_b \left\{ \frac{aL_9}{1+\nu} - r\,G_6(r) + \frac{\sigma_b h^2 \nu}{6aL_9}\left[aL_9 - r\,G_9(r) \right] \right\} \right) ,$$

where ν is the Poisson ratio, L_9 is the Roark and Young plate function,[1]

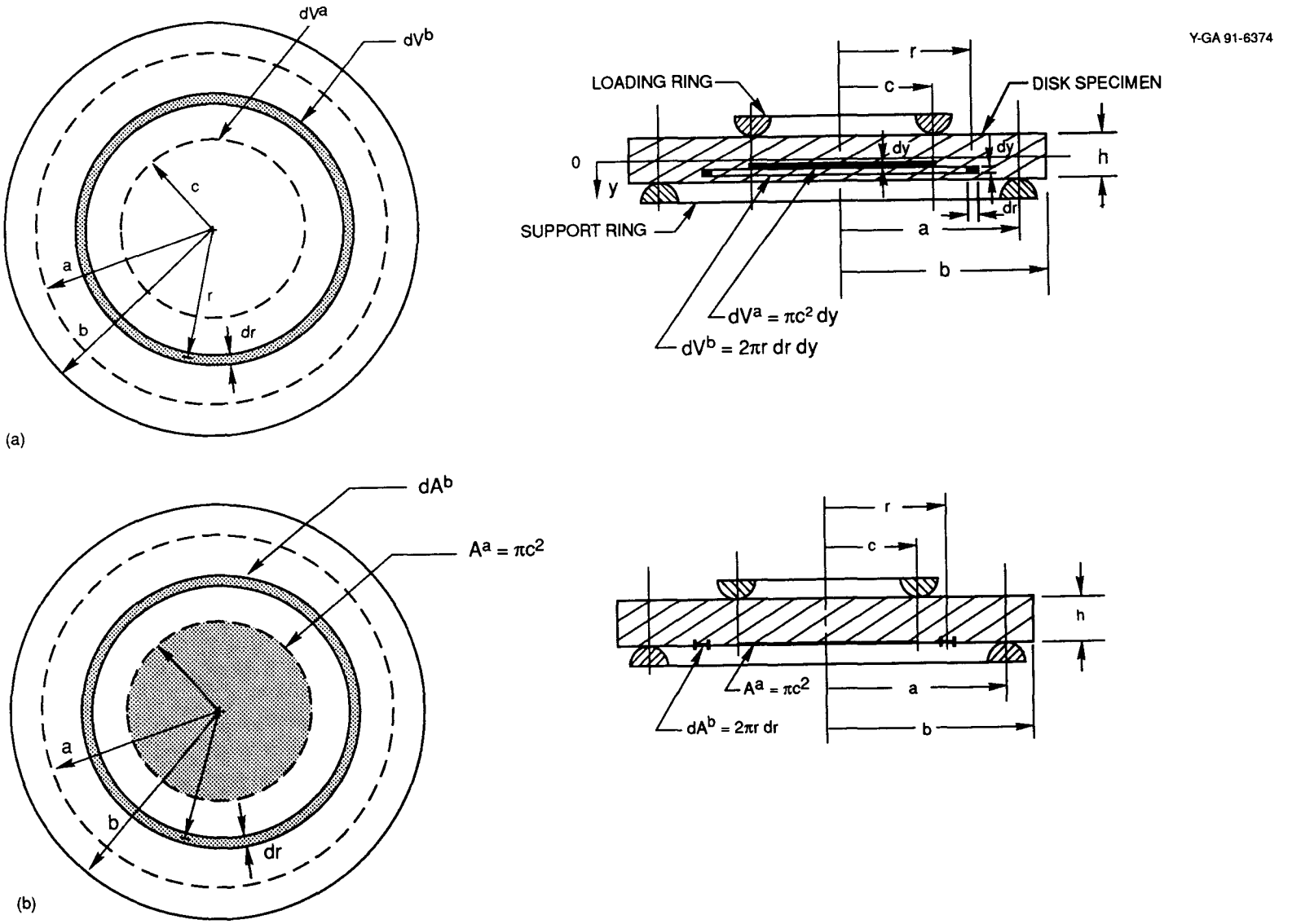

Fig. C.1. Definition of volume and surface elements used to derive effective volume and area for the biaxial-disk-flexure specimen. (a) Disk and ring volume elements used for risk-of-rupture integrations for center and outer regions of specimen; and (b) inner effective area and outer ring area element used for risk-of-rupture integration for outer region of specimen.

$$L_9 = \frac{c}{a}\left\{\frac{1+\nu}{2}\ln\frac{a}{c} + \frac{1-\nu}{4}\left[1 - \left(\frac{c}{a}\right)^2\right]\right\},$$

and $G_6(r)$ and $G_9(r)$ are variable functions of the radius, r, defined as

$$G_6(r) = \frac{c}{4r}\left[\left(\frac{c}{r}\right)^2 - 1 + 2\ln\frac{r}{c}\right]$$

and

$$G_9(r) = \frac{c}{r}\left\{\frac{1+\nu}{2}\ln\frac{r}{c} + \frac{1-\nu}{4}\left[1 - \left(\frac{c}{r}\right)^2\right]\right\}.$$

The risk of rupture for the outer region is

$$B^b = \int_V \left[\frac{\sigma^b(r,y)}{\sigma_0}\right]^m dV^b .$$

If we use the volume element $dV^b = 2\pi r\, dr\, dy$ of Fig. C.1 and the tangential-stress component σ_t^b, the risk of rupture becomes

$$B_t^b = 2\pi\left[\frac{2(1-\nu^2)}{haL_9}\right]^m\left(\frac{\sigma_b}{\sigma_0}\right)^m \int_{r=c}^{a}\int_{y=0}^{h/2} y^m \left\{\frac{aL_9}{1+\nu} - r\,G_6(r) + \frac{h^2\nu}{6aL_9}\left[aL_9 - r\,G_9(r)\right]\right\}^m r\,dr\,dy,$$

which involves two variables requiring integration in parts. Rearranging as

$$B_t^b = 2\pi\left[\frac{2(1-\nu^2)}{haL_9}\right]^m\left(\frac{\sigma_b}{\sigma_0}\right)^m \int_{r=c}^{a}\left(\left\{\left[\frac{aL_9}{1+\nu} - r\,G_6(r)\right] + \frac{h^2\nu}{6aL_9}\left[aL_9 - r\,G_9(r)\right]\right\}^m \int_{y=0}^{h/2} y^m\,dy\right) r\,dr$$

separates the variables, and the second integral in the above equation can be solved in closed form as

$$\int_{y=0}^{h/2} y^m \, dy = \frac{(h/2)^{m+1}}{m+1} .$$

The first integral requires numerical integration, so the risk of rupture for the outer region reduces to

$$B_t^b = 2\pi\left(\frac{1-\nu^2}{aL_9}\right)^m \frac{h}{2(m+1)} \left(\frac{\sigma_b}{\sigma_0}\right)^m \int_{r=c}^{a} \left\{\left[\frac{aL_9}{1+\nu} - r\,G_6(r)\right] + \frac{h^2\nu}{6aL_9}\left[aL_9 - r\,G_9(r)\right]\right\}^m r\,dr ,$$

which, after being divided by the stress function $(\sigma_b/\sigma_0)^m$, becomes the effective volume for the outer region of the biaxial-disk specimen,

$$V_t^b = 2\pi\left(\frac{1-\nu^2}{aL_9}\right)^m \frac{h}{2(m+1)} \int_{r=c}^{a} \left\{\left[\frac{aL_9}{1+\nu} - r\,G_6(r)\right] + \frac{h^2\nu}{6aL_9}\left[aL_9 - r\,G_9(r)\right]\right\}^m r\,dr . \qquad \text{(C.2)}$$

Finally, the total effective volume for the biaxial-disk-flexure specimen, $V_{E,BDF}$, is the sum of Eqs. (C.1) and (C.2),

$$V_{E,BDF} = \frac{\pi h c^2}{2(m+1)} + 2\pi\left(\frac{1-\nu^2}{aL_9}\right)^m \frac{h}{2(m+1)} \int_{r=0}^{a} \left\{\frac{aL_9}{1+\nu} - r\,G_6(r) + \frac{h^2\nu}{6aL_9}\left[aL_9 - r\,G_9(r)\right]\right\}^m r\,dr .$$

THE EFFECTIVE AREA

The effective area of the biaxial-disk-flexure specimen, $A_{E,BDF}$, like the effective volume, is composed of two distinct regions, the region within the inner ring (superscript *a*) and the region between the inner and the outer loading ring (superscript *b*).

Within the inner ring, the outer-surface equibiaxial stress is constant and equals the reported stress, σ_b; thus, the effective area is simply the area of the circle,

$$A_{E,BDF}^a = \pi c^2 \quad \textit{(center region)} .$$

Between the inner and outer supports, the larger tangential surface stress in terms of the reported strength σ_b is a function of r,

$$\sigma_t^a(r) = \frac{\sigma_b}{aL_9}\left[aL_9(1 - \nu) - r\,G_6(r)\,(1 - \nu^2) + \frac{aL_9h^2\nu}{6} - \frac{h^2r\,G_9(r)\,\nu}{6}\right],$$

where $G_6(r)$, $G_9(r)$, and L_9 are as previously defined.

If we use the surface element $dA^b = 2\pi r\,dr$ of Fig. C.1, the risk of rupture for the outer area is

$$B^b = \int_V \left[\frac{\sigma(r)}{\sigma_0}\right]^m dA^a = \int_{r=c}^{a} \left\{\frac{\sigma_b}{aL_9}\left[aL_9(1-\nu) - r\,G_6(r)\,(1-\nu^2) + \frac{aL_9h^2\nu}{6} - \frac{h^2r\,G_9(r)\,\nu}{6}\right]\right\}^m 2\pi r\,dr,$$

which, after being rearranged and divided by the stress function $(\sigma_b/\sigma_0)^m$, becomes the effective area for the outer region,

$$A^b_{E,BDF} = \frac{2\pi}{a^m L_9^m}\int_{r=c}^{a}\left\{aL_9(1-\nu) - r\,G_6(r)\,(1-\nu^2) + \nu\frac{h^2}{6}\left[L_9 - r\,G_9(r)\right]\right\}^m r\,dr.$$

The total effective area for the biaxial-disk-flexure specimen, $A_{E,BDF}$, is the sum of $A^a{}_{E,BDF}$ and $A^b{}_{E,BDF}$,

$$A_{E,BDF} = \pi c^2 + \frac{2\pi}{a^m L_9^m}\int_{r=c}^{a}\left\{aL_9(1-\nu) - r\,G_6(r)\,(1-\nu^2) + \nu\frac{h^2}{6}\,[L_9 - r\,G_9(r)]\right\}^m r\,dr, \qquad \text{(C.3)}$$

which requires numerical integration for evaluation.

REFERENCE

1. R. J. Roark and W. C. Young, *Formulas for Stress and Strain*, McGraw-Hill Book Company, New York, 1975.

APPENDIX D

LITHIUM HYDRIDE TENSILE STRENGTHS FROM FOUR SPECIMEN TYPES

Four-point flexure (MPa)		Ring tensile (MPa)	Elliptical-transition tensile (MPa)	Axial-disk flexure (MPa)
Large	Small			
−17.5[a]	51.4	−10.1[a]	−16.9[a]	−14.7[a]
−20.4	51.6	−10.1	−21.9	−18.1
−25.9	53.8	−12.0	29.1	−18.3
−25.4	56.3	−16.8	30.1	−20.5
−26.2	56.7	−19.0	33.9	21.0
−28.2	61.2	−21.8	34.0	21.0
−30.4	61.6	−22.1	35.2	21.4
−30.6	61.8	−23.8	36.5	21.5
−32.4	66.4	−25.6	36.5	22.1
−32.6		−31.1	36.9	22.7
−32.7		−32.7	41.3	22.8
−33.2		−33.1		22.8
−36.1		−34.9		22.9
−36.4		−35.3		23.3
−36.8		−35.6		23.3
−37.0		−36.0		23.4
−37.2		36.4		23.8
−37.3		37.1		24.3
−38.8		37.5		24.8
−39.0		38.0		24.8
−39.4		38.8		24.8
−39.6		38.9		24.8
39.9		39.1		25.2
41.0		41.0		25.4
42.1		41.0		25.6
42.6		42.9		25.6
42.8		43.5		25.6
43.3		44.0		25.9
45.5		44.8		26.6
47.9		44.9		26.9
48.0		48.3		27.1
50.1		50.4		27.4
50.4				27.8
55.0				27.8
				28.0
				28.2
				30.2

[a] Negative values indicate suspended data points associated with surface-initiated failures; positive values are associated with internally initiated failures.

DISTRIBUTION:

EG&G Rocky Flats

1. S. Beitscher

Lawrence Livermore National Laboratory

2. R. M. Alire
3. R. L. Barber
4. R. Brady
5. T. O. Dalrymple
6. Elaine Flower
7. L. G. Hangartner
8. R. Hatfield
9. C. L. Hoenig
10. R. L. Landingham
11. D. Lesuer
12. W. Moen
13. D. L. Seaton
14. Dave Selway
15. Technical Information Center
16. R. L. Woelffer

Los Alamos National Laboratory

17. W. R. Doty
18. L. E. Edwards
19. D. J. Hayden
20. R. E. Hunter
21. George Hurley
22. T. E. Larson
23. Library Services
24. Richard Macek
25. D. P. MacMillian
26. R. L. Nolen
27. G. E. Seay
28. J. B. Straw
29. G. W. Taylor

Mason and Hanger-Silas Mason

30. G. L. Flowers
31. Herb Johnson

Oak Ridge National Laboratory

32. C. R. Brinkman
33. K. C. Liu
34. A. C. Shaffhauser

Oak Ridge Y-12 Plant

35. W. D. Babb
36. R. Baylor
37. S. W. Bidinger
38. W. L. Bolinger
39. G. L. Bowers
40. S. W. Brown
41. R. B. Burditt
42. T. R. Butler
43. T. R. Chilcoat
44. C. M. Davenport
45. J. M. Googin
46. T. R. Harvey
47. C. E. Holcombe
48. P. J. Horton
49. A. H. Hunter
50. D. H. Johnson
51. F. W. Jones
52. M. D. Kass
53. J. D. Kennedy
54. K. A. Kitzke
55. R. Krabill
56. S. C. Laggis
57. M. J. Marsicek
58. J. F. McLaughlin
59. S. R. Minge
60. C. D. Montgomery
61. W. G. Northcutt
62–73. R. E. Oakes
74. D. R. Passons
75. M. W. Poore
76. D. A. Ray
77. C. D. Reynolds
78. R. C. Riepe
79. P. A. Sadler

80. P. G. Schneider
81. W. E. Steinkamp
82. L. D. Snow
83. R. G. Vornehm
84. D. Waldrop
85. W. J. Werner
86–89. Y-12 Central Files

U. S. Department of Energy

90–195. OSTI*

*Given distribution as shown in DOE/OSTI-4500 under Category UC-704, *Materials* (106 copies).